Reduction of mechanical losses in ion-beam sputtered tantalum oxide thin films via partial crystallization

OPEN ACCESS
IOP Publishing
Classical and Quantum Gravity
Class. Quantum Grav. **41** (2024) 105009 (15pp)
https://doi.org/10.1088/1361-6382/ad3c8a

Reduction of mechanical losses in ion-beam sputtered tantalum oxide thin films via partial crystallization

Giulio Favaro[1,*], Valeria Milotti[1], Diego Alonso Diaz Riega[1], Nicole Busdon[1], Marco Bazzan[1,*], Massimo Granata[2], David Hofman[2], Christophe Michel[2], Laurent Pinard[2], Livia Conti[3], Simone Capaccioli[4,5], Nikita S Shcheblanov[6,7], Anaël Lemaître[6,7], Valérie Martinez[8], Gianpietro Cagnoli[8], Francesco Piergiovanni[9,10], Federica Fabrizi[9,10], Maria G Pelizzo[11] and Alain J Corso[12]

[1] Dipartimento di Fisica e Astronomia, Universitá di Padova, via Marzolo, 8, 35131 Padova, Italy
[2] Laboratoire des Matériaux Avancés—IP2I, CNRS, Université de Lyon, F-69622 Villeurbanne, France
[3] INFN Padova, Via Marzolo 8, 35131 Padova, Italy
[4] Dipartimento di Fisica, Universitá di Pisa, Largo Bruno Pontecorvo 3, Pisa I-56127, Italy
[5] CISUP, Centro per l'Integrazione della Strumentazione dell'Universitá di Pisa, Lungarno Pacinotti 43, Pisa I-56127, Italy
[6] Navier, UMR 8205, Ecole des Ponts ParisTech, Univ. Gustave Eiffel, CNRS, Marne-la-Vallée, France
[7] MSME, UMR 8208, Univ. Gustave Eiffel, CNRS, Univ. Paris-Est Créteil, Marne-la-Vallée, France
[8] Institut Lumière Matière, UMR5306 CNRS Université Claude Bernard Lyon 1, Villeurbanne, France
[9] Universitá di Urbino, Via S.Chiara 27, 61029 Urbino, Italy
[10] INFN Firenze, Via Sansone 1, 50019 Sesto Fiorentino, Italy
[11] Dipartimento di Ingegneria dell'Informazione, Universitá di Padova, via Gradenigo, 6B, 35131 Padova, Italy
[12] Consiglio Nazionale delle Ricerche—Istituto di Fotonica e Nanotecnologie (CNR-IFN), via Trasea, 7, 35131 Padova, Italy

[*] Authors to whom any correspondence should be addressed.

E-mail: giulio.favaro@phd.unipd.it and marco.bazzan@unipd.it

Received 31 December 2023; revised 11 March 2024
Accepted for publication 9 April 2024
Published 24 April 2024

Abstract

This study explores the impact of crystalline fraction on the mechanical losses of amorphous tantalum oxide (tantala, Ta_2O_5) thin films intended for gravitational wave detectors. We use ion beam sputtering technique to prepare a series of samples, which are then subjected to controlled thermal annealing to achieve varying degrees of crystallized fraction. The microscopic structure of the annealed samples is characterized by combining different analytical techniques. Our investigation reveals that the amorphous films comprise randomly distributed crystalline grains, whose density and average size depends on the duration of thermal treatment. To assess mechanical losses of the coatings, a gentle nodal suspension system is applied. Remarkably, a substantial reduction of approximately 20% in the coating's mechanical loss angle with respect to annealed amorphous coatings is observed for samples exhibiting a crystalline fraction of around 5%. This improvement may lead to the definition of alternative thermal treatments to improve the mechanical performances of coatings for gravitational wave detectors or other highly sensitive optical experiments. However the reduction in mechanical losses comes at the expense of an increase in optical scattering. The possibility of reducing the optical losses to the level required by gravitational interferometers by modifying the grain size distribution via appropriate annealing treatments is discussed.

Supplementary material for this article is available online

Keywords: mirror coatings, gravitational waves, thermal noise, crystallization, scattering

1. Introduction

Second-generation gravitational-wave (GW) detectors are km-size Michelson interferometers with Fabry–Perot cavities inside their arms [1–3]. The mirrors of those instruments are made of super-polished, highly transparent test masses whose surface is coated with high-reflectivity stacks of alternating low-refractive index (LI) and high-refractive index (HI) materials, designed to work as Bragg reflectors at the operating wavelength of the detector. Currently, the GW interferometers LIGO in the USA [1], VIRGO in Italy [2] and KAGRA [3] in Japan use amorphous layers of SiO_2 as LI material and Ti-doped Ta_2O_5 as HI one, both deposited by means of an ion beam sputtering (IBS) technique. Future third-generation detectors such as Einstein Telescope [4] and Cosmic Explorer [5] will likely use similar technologies [6, 7] (see also [8] for a review on the properties of those materials).

Mirror coatings play a pivotal role in the performance of GW interferometers, especially in the most-sensitive frequency band of the interferometers (∼40–400 Hz), where the coating Brownian thermal noise (CTN) sets the detection limit CTN is due to the presence of random fluctuations of the atomic structure in the coating layers occurring at finite temperature [9, 10]. Those random structural rearrangements can be related, via the fluctuation-dissipation

theorem [11], to the rate of energy dissipation in the coating material as measured by its mechanical loss angle φ_c. In particular, HI layers of Ti-doped Ta_2O_5 provide the main contribution to the thermal noise floor of the current interferometers. For this reason, a worldwide effort [12] is being carried out to design and optimize optical HI coatings characterized by a low level of thermal noise, i.e. low mechanical losses.

In recent times, *crystalline* coatings are emerging as a promising alternative for use in GW detectors [13]. These coatings are characterized by a mechanical loss angle, which is one order of magnitude smaller than that of amorphous HI materials. However producing large-size crystalline thin film layers and then transferring them onto the test masses while preserving their exceptional opto-mechanical qualities is a major technological challenge [12]. Crystalline regions can also be produced inside amorphous optical coatings by performing thermal annealing at sufficiently high soaking temperatures and for sufficiently long times. However in this case the presence of crystalline regions is commonly considered as detrimental as it would originate unwanted optical scattering. Yet, to the best of our knowledge, there are no systematic studies on the effect of crystalline regions in the mechanical properties of amorphous films.

In this work we investigate quantitatively this poorly known feature by correlating the amount of crystalline fraction in an amorphous Ta_2O_5 layer to its mechanical losses thus progressing in the assessment of the feasibility of this option for lowering the thermal noise of GW detectors. The samples are produced by mimicking the fabrication conditions of standard coatings for GW detectors (see [8]) and annealed at a suitable temperature for different times to produce different amounts of partial crystallization. The crystalline fraction is studied by means of optical microscopy coupled with Grazing-Incidence x-ray Diffraction and micro-Raman mapping. Finally the impact of crystallization on optical scattering and mechanical loss is investigated by means of a spectrophotometer equipped with an integrating sphere and with a gentle nodal suspension (GeNS) system, respectively. Our study indicates that a moderate amount of crystalline regions may induce a substantial reduction of the coating mechanical losses, at the cost of an increase of scattering losses. The implementation of this approach for producing low-noise optical coatings is discussed.

2. Sample preparation

Coatings were deposited at LMA-IP2I, Lyon (France) by using IBS technique. The energy and current of the Ar sputtering ions were 1.25 keV and 0.6 A, respectively, yielding an average coating deposition rate of 2.85 ± 0.04 nm s^{-1}. The total pressure during the coating process was of the order of 10^{-4} mbar, with 21 sccm of Ar and 37 sccm of O_2 injected into the chamber.

In different deposition runs, ∼500 nm thick layers of IBS Ta_2O_5 were deposited on:

(i) several 75 mm diameter, 0.35 mm thick disks of Corning 7980 A fused-silica;
(ii) several 75 mm diameter, 0.5 mm thick, single-side-polished, (100) p-doped silicon wafers;
(iii) one 75 mm diameter, 1 mm thick disk of Corning 7980 A fused silica for coating loss angle measurements. Prior to coating deposition, this thicker fused-silica disk was annealed in air at 900 °C for 10 h in order to release its internal stress due to manufacturing and to minimize its intrinsic loss angle φ_0 [14]. The coating was then deposited on both surfaces, in two consecutive coating runs, performed under identical conditions, in order to cancel out any potential curvature effect that might affect its mechanical mechanical response.

After deposition, as part of the standard production procedure, all samples were thermally treated at 500 °C in air for 10 h to reduce mechanical stresses in the coating and favor its

Table 1. Soaking temperature and time (hours) of successive annealing steps applied to samples from series (ii), together with the crystalline fraction measured by optical microscopy. Heating and cooling ramps of $100\,^{\circ}\mathrm{C\,h^{-1}}$ were used.

Sample	Step 0	Step 1	Step 2	Step 3	Step 4	Step 5	Crystalline fraction
K0	10 h, 500 °C	—	—	—	—	—	0
K1	10 h, 500 °C	6 h, 630 °C	—	—	—	—	$(0.05 \pm 0.03)\%$
K2	10 h, 500 °C	6 h, 630 °C	3 h, 630 °C	—	—	—	$(0.84 \pm 0.15)\%$
K3	10 h, 500 °C	6 h, 630 °C	3 h, 630 °C	3 h, 630 °C	—	—	$(4.7 \pm 0.6)\%$
K4	10 h, 500 °C	6 h, 630 °C	3 h, 630 °C	3 h, 630 °C	3 h, 630 °C	—	$(10.3 \pm 0.6)\%$
K5	10 h, 500 °C	6 h, 630 °C	3 h, 630 °C	3 h, 630 °C	3 h, 630 °C	3 h, 630 °C	$(28.3 \pm 3.0)\%$

relaxation. This thermal treatment step is common to all our samples and does not induce any evidence of crystallization [8].

Thermal treatments (hereinafter *annealing*) were carried out in a Carbolite CTF 12/75/700 oven in ambient atmosphere. First, samples of series (i) were annealed to determine a suitable working point. From these preliminary tests, we decided to use incremental annealing steps performed at a constant plateau temperature of 630 °C. We thus prepared a set of samples K1 –K5, each of them being treated by an incremental number of subsequent treatments. For all annealing steps, the heating and cooling ramps used were controlled to $100\,^{\circ}\mathrm{C\,h^{-1}}$. Table 1 lists the samples of series (ii) with their respective treatments used for optical, GIXRD and total integrated scattering measurements, to which we assign the serial numbering $i = 0, \ldots, 5$. The remaining sample, the one of series (iii) for coating loss angle measurement, underwent annealing steps 1 to 3 and then step 5. In this case a single sample was characterized for loss angle before and after each annealing step. We performed the sensitive mechanical loss measurements immediately after the thermal treatment, in order to avoid any spurious, uncontrolled ageing effect [15].

3. Experimental results

3.1. Optical microscopy

Visual inspection of sample surfaces was carried out using a Keyence VHX-7000 digital microscope. Samples were illuminated with coaxial lighting and a pair of polarizing filters was placed in the optical path.

Digital microscope images for K samples are shown in figures 1(a)–(e). All the images demonstrate a uniform background with some randomly distributed grains of different colors. The average size and areal density of the grains increase with increasing annealing time. The detected color and intensity of light reflected from the grains is dependent on the relative orientation of the polarization filters, while the uniform background appears unchanged under the same conditions (see figure S.1 in the supplementary information). From these observations we infer that the uniform background represents the areas where the coating is still in its amorphous phase, while grains represent optically anisotropic regions where the Ta_2O_5 coating is locally crystallized.

In order to quantify the crystallization process, we performed a particle count analysis on pictures with an area of $50 \times 50\,\mu\mathrm{m}^2$ taken at several spots on each sample. This gave us a statistically significant estimate for the crystalline fraction of the coating volume, reported in

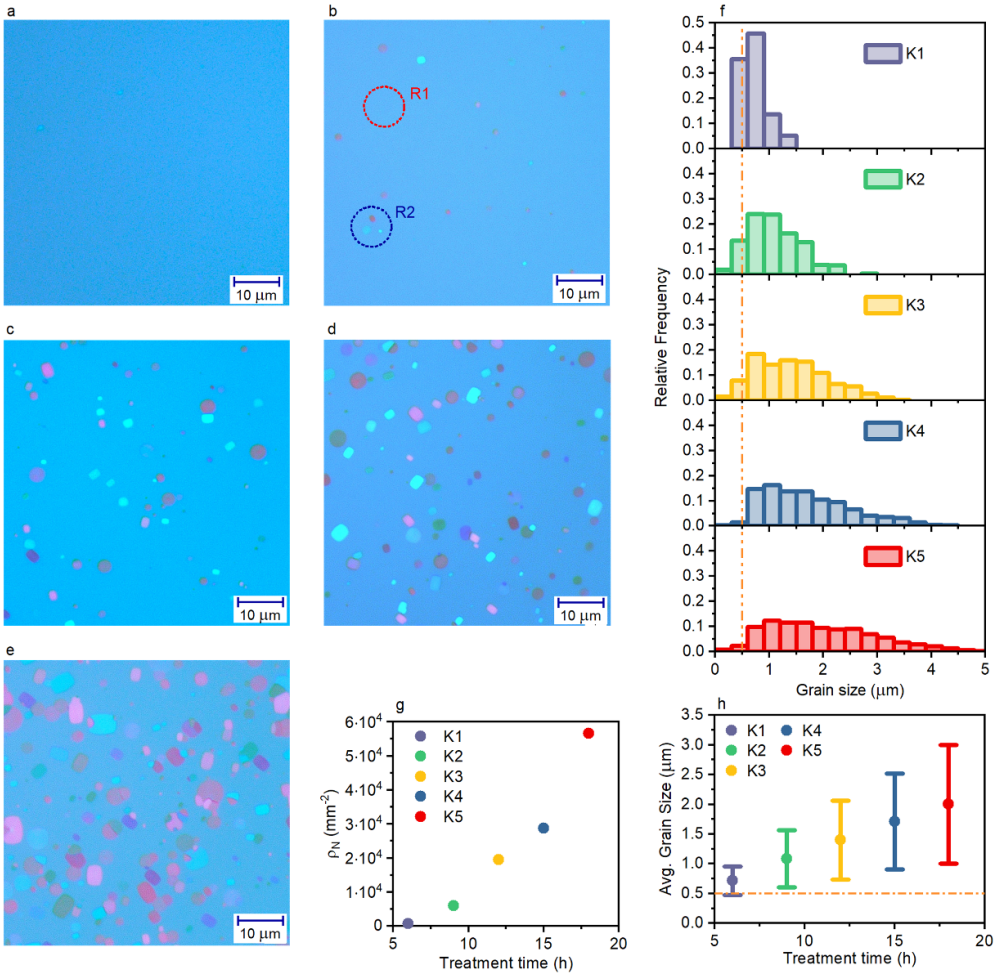

Figure 1. Optical microscope images taken with polarizing filters of samples (a) K1, (b) K2, (c) K3, (d) K4 and (e) K5. (f) Relative frequency distributions of grain size detected by optical microscopy. Crystal grain areal density ρ_N (g) and average grain size (h) against total annealing time at 630 °C. The circled areas R1 and R2 in (b) indicate two regions without and with visible grains, respectively. Orange lines in (f) and (h) show the comparison with coating film thickness.

table 1: the crystalline fraction is below 1% for samples annealed less than 9 h (K1 and K2), while it grows dramatically in samples with longer annealing times. This analysis also allowed us to quantitatively estimate the size distribution and areal density of grains ρ_N for each sample. We calculated the grain size as the square root of measured grain areas, in order to remove differences due to grain shape. The size distribution of grains for each sample, normalized to 1 to provide the relative frequency, is reported in figure 1(f), while the average grain size and the crystal grain areal density as a function of the treatment duration are reported in figures 1(g) and (h), respectively.

The distribution in figure 1(f) resembles grain size distributions of crystallization models reported in previous studies [16]. Already for K1, the least crystallized sample, the average crystal size is larger than the coating film thickness, which is about 500 nm (orange dotted line

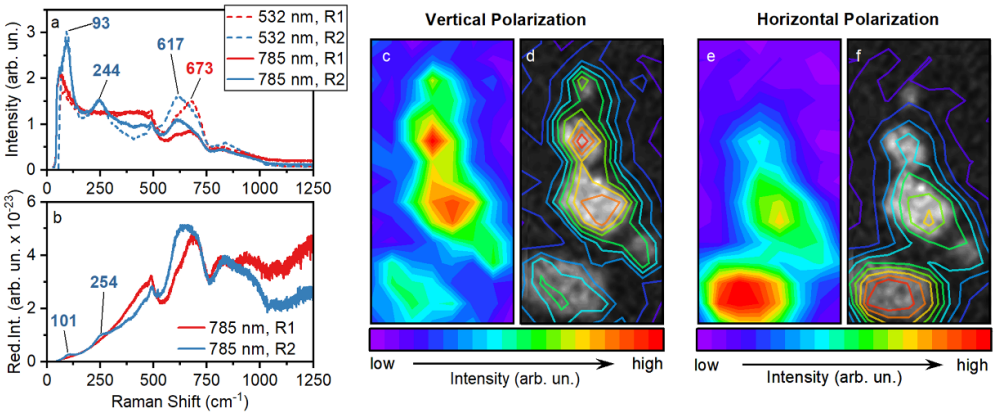

Figure 2. (a) Raman spectra of R1-like and R2-like regions acquired at 532 and 785 nm. (b) Corresponding reduced Raman spectra at 785 nm. (c)–(f) R2-like region with five individual grains, as observed via optical microscopy and Raman maps at 532 nm: panels (c) and (e) show relative intensity maps of the 244 m^{-1} feature with vertical and horizontal polarizations, respectively; panels (d) and (f) show the intensity maps of panels (c) and (e) overlapped with an optical microscopy image of the corresponding region.

in figures 1(f) and (h)). Thus, crystal growth at very early stages is limited to two-dimensional growth.

3.2. Micro-Raman spectroscopy

We characterized the vibrational properties of the samples with a Horiba XploRA Plus spectrometer, at exciting laser wavelengths of 532 nm and 785 nm. We used samples from series (i) for the Raman characterization, as the background signal from the SiO_2 substrate was much smaller than that of the Si substrate of samples K from series (ii). We focused on the differences between homogeneous-looking areas and areas where one or more grains were visible, such as regions R1 and R2 in figure 1(b), respectively.

The resulting Raman spectra are shown in figure 2(a). The signal from region R1 shows a Ta_2O_5-related feature at 673 cm^{-1} and is otherwise dominated by signal from the SiO_2 substrate. Conversely, new features are visible in the R2 spectrum, with peaks arising at 93, 245 and 617 cm^{-1}. The peak at 673 cm^{-1} is not visible in R2 case, at least not as a resolved individual feature. Signal from SiO_2 is present also in this case, although it is much less relevant than in R1 case. Comparison between the 532 nm and 785 nm signal shows the Ta_2O_5 spectral features are not changed in shape or position, with the only major difference given by a change of background signal between $\sim$500 and 1000 cm^{-1} . This latter effect can be due either to an actual quenching of fluorescence signal from the SiO_2 substrate or to a variety of wavelength-dependent instrumental effects such as etalon interference due to the thin-film geometry, a change of the confocal optical probe size along the surface normal , etc. The consistency of the Ta_2O_5 spectra allows us to study it with either laser wavelength. Notably, the spectra gathered from R1 and R2 regions are consistent with the reported spectra from amorphous and crystalline Ta_2O_5, respectively [17, 18]. This confirms that the grains with different refractive index contrast are indeed crystalline grains of Ta_2O_5 embedded in an amorphous matrix.

In order to gain a clearer picture of the vibrational density of states and Raman coupling, we represented the spectra into their reduced form as follows [19]:

$$\mathcal{I}_R(\omega) = \omega(\omega_L - \omega)^{-4}[n(\omega)+1]^{-1}\mathcal{I}_0(\omega)\,, \tag{1}$$

where $\mathcal{I}_0(\omega)$ is the experimentally determined intensity, ω_L is the incident laser frequency, and $n(\omega)$ is the following temperature-related boson factor:

$$n(\omega) = [\exp(\hbar\omega/k_BT) - 1]^{-1}\,. \tag{2}$$

$\mathcal{I}_R(\omega)$ can be represented as $\mathcal{I}_R(\omega) = C(\omega)\rho(\omega)$, where $C(\omega)$ is the coupling function and $\rho(\omega)$ is the vibrational density of states (VDOS). The reduced spectrum is thus proportional to the VDOS, providing a spectrum not affected by particular measurement conditions such as the sample temperature and incident laser frequency. The reduced spectra for 785 nm are shown in figure 2(b). The previously observed shift of the peak at around 600 cm^{-1} between R1 to R2 cases is confirmed, as is the presence of spectral features at low wavenumbers, though their spectral position is changed. Non-linear peak fitting shows that the new positions for the peaks, which we observed at 93 cm^{-1} and 244 cm^{-1} in figure 2(a), are 101 cm^{-1} and 254 cm^{-1}, respectively. These latter two values are therefore corresponding to the true position of these features in the VDOS and coupling.

Furthermore, we studied the dependence of the Raman response of the crystalline grains with respect to the polarization direction of the the incident laser beam. We identified a region with several grains which was studied by performing a Raman spectral mapping on a grid-like pattern. By examining the relative intensity in each spectra of grain-related peaks identified in figure 2(a), we obtained the spatial intensity distribution for each spectral feature. We repeated this process for two incident laser polarizations, horizontal and vertical, which are rotated 90° with respect to one other. We acquired the intensity maps at 532 nm rather than at 785 nm because of the higher signal-to-noise ratio.

Figures 2(c) and (e) show the relative intensity maps of the peak at 244 cm^{-1} for vertical and horizontal polarizations, respectively. If the maps are superimposed on the optical microscope image (figures 2(d) and (f)), we can see that the intensity map reproduces the position of the grains. However, the signal from different grains clearly depends on the input polarization used.

The different response to polarized light allows us to conclude that each grain is nearly single-crystalline, with different crystallographic orientations with respect to each other in agreement with the observations in polarized-light microscopy reported in figure S.1.

3.3. Grazing incidence x-ray diffraction

Grazing incidence x-ray diffraction (GIXRD) measurements were performed to provide further confirmation that the grains identified by optical microscopy and Raman spectroscopy are indeed cristalline. We used a PANalytical MRD Diffractometer equipped with a Cu tube operated at 40 kV, 40 mA. The CuK_α radiation ($\lambda = 1.540\,56$ Å) was collimated and monochromatized with the help of a parabolic multilayer mirror and a slit. As detector, we used a Xe proportional counter equipped with a parallel plate collimator mounted in front of it, providing an angular acceptance in the scattering plane of about 0.1 degrees. Furthermore, a Soller slit was inserted in order to limit the axial acceptance to 0.04 radians. The grazing incidence

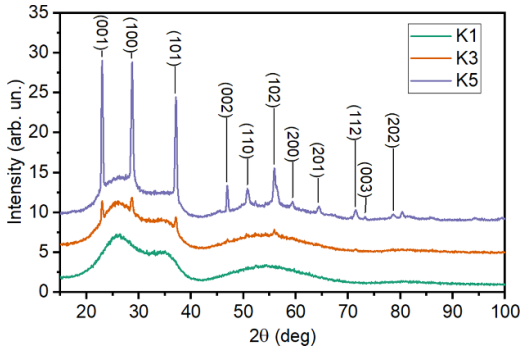

Figure 3. GIXRD spectra of samples K1, K3 and K5. The main peaks are indexed to the hexagonal phase of Ta_2O_5.

configuration was chosen in order to enhance the scattering signal from the thin film. The diffraction spectrum for all samples was measured by keeping the primary beam fixed at an incidence angle of 1° with respect to the sample surface and moving the detector goniometer (2θ-scan) with 2θ ranging from 15° to 100° (see figure 3).

Diffraction spectra for samples K1, K3 and K5 are reported in figure 3. The spectrum for K1 does not show any sharp features, which is consistent with the spectrum of amorphous Ta_2O_5. On the other hand, well-defined diffraction peaks are visible in the spectrum for K5. The same features are visible in the K3 spectrum, which represents an intermediate case between K1 and K5, where the peaks appear above the background but are still low in intensity. From the width of the diffraction peaks (corrected for the instrumental broadening by means of a LaB_6 calibration standard) it is possible to determine the average diffraction domain size, which for sample K5 is about 80 Å. This is close to the maximum size that can be detected by using this method, indicating that the grains are characterized by a long-range crystalline perfection. The obtained diffraction spectra are in good agreement with the ones reported by other authors for crystallized Ta_2O_5 [20–22]. The main features of diffraction pattern can be indexed to the hexagonal phase Ta_2O_5 (JCPDS No. 19-1299), as reported in the above-mentioned papers.

The intensity of the diffraction peaks is directly related to the crystalline fraction in samples K1, K3 and K5, providing further confirmation that the structures observed in sections 3.1 and 3.2 are indeed a collection of crystalline grains dispersed in the amorphous coating matrix. To perform a more quantitative analysis, one of the samples from series (i) was treated for 100 h at 630 °C to obtain a fully crystallized sample. Then a set of samples from series (i), treated with different duration in order to induce a partial crystallization, were measured by GIXRD. Assuming that the peak intensity at $2\theta = 28°$ is proportional to the crystallized volume, we estimated the crystalline fraction from the GIXRD spectra by normalizing the various measurements with respect to the peak intensity of the fully crystallized sample. The same samples were also measured by using optical microscopy according to the protocol described in section 3.1 to obtain an independent estimate of the crystalline fraction of the coating. The two estimates are in very good agreement, as it can be seen from values reported in table S.I in the supplementary information. Thus, we confirmed that the optical measurement of the crystalline fraction is reliable and even more sensitive than GIXRD, since crystalline grains can be detected even when they are very rare, as in the case of sample K1.

Table 2. Mass of the fused-silica disk used in coating loss angle measurements, as measured before (m_0) and after (m) coating deposition.

m_0 (g)	m (g)	$m - m_0$ (g)
10.2872 ± 0.0005	10.3167 ± 0.0004	0.0295 ± 0.0006

3.4. Loss angle measurements

The sample from series (iii) was used for coating loss angle measurements. This sample underwent the same annealing steps 1 to 3 and then step 5 of table 1, thus we can safely assume that after each step it featured the same crystalline fraction of samples K of series (ii). Its coating loss angle was measured before and after the coating deposition as well as after each annealing step, as described in the following. We used an experimental apparatus based on the ring-down technique [23] to measure the frequency f and ring-down time τ of several disk resonant modes, and calculated the coating loss angle φ_c as

$$\varphi_c = \frac{\varphi - (1-D)\,\varphi_0}{D}\,, \tag{3}$$

where φ_0 and φ are the loss angles associated to the internal friction of the bare disk and of the coated disk, respectively, and D is the so-called *dilution factor* defined as [24]

$$D = 1 - \frac{m_0}{m}\left(\frac{f_0}{f}\right)^2\,, \tag{4}$$

where f_0, f, m_0 and m are the disk resonant frequency and mass as measured before and after coating deposition, respectively. We measured the sample mass with an analytical balance, before and after each treatment (coating deposition, annealing steps), and observed that it remained constant after the coating deposition, that is, the annealing steps never changed it. The measured mass values are reported in table 2.

In order to avoid systematic damping from suspension and ambient pressure, we used a clamp-free in-vacuum GeNS system [25] in our ring-down apparatus. Resonant modes were measured from ∼2.5 to ∼20 kHz, in a frequency band partially overlapping with that of ground-based gravitational-wave interferometers (10–10^4 kHz). Figure S.2 shows the measured loss angles φ_0 and φ of the bare substrate and coated sample, respectively, where the typical uncertainties of the order of 10% for φ_0 and of the order of 1% for φ were obtained from three independent suspensions of the sample.

Indeed, according to equation (4), the estimation of the dilution factor and hence of the coating loss angle via equation (3) depends critically on the resonant frequency of the sample modes, which in turn depend on the sample temperature; if the temperature is not constant throughout all measurement steps, a systematic error is introduced [26]. Thus, whenever we observed a temperature difference $\Delta T = T - T_0$ between measurement steps, we estimated the induced systematic frequency error as

$$\Delta f = \frac{\eta}{2} f_0\,\Delta T\,, \tag{5}$$

where $f_0 \equiv f(T_0)$ is taken as the reference value, and $\eta = (1.50 \pm 0.01) \times 10^{-4}\ {}^\circ\mathrm{C}^{-1}$ [26], subtract it from measured resonant frequencies and used the corrected values in equation (4). The obtained coating loss angle φ_c are reported in figure 4(a), as a function of frequency, where

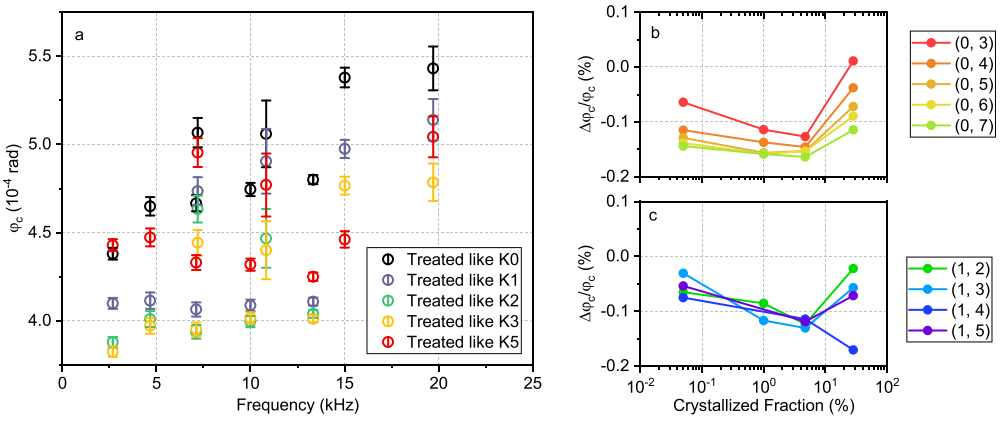

Figure 4. (a) Coating loss angle of disk from sample series (iii) as a function of frequency, as measured after annealing. Relative loss angle of (b) butterfly modes and (c) mixed modes vs. crystalline fraction.

the uncertainty is a standard deviation obtained by propagating the uncertainties on measured values of resonant frequencies, mass and loss angles φ_0 and φ.

In order to highlight the changes brought upon by the amount of crystalline fraction, we define the relative coating loss angle variation after the annealing step i as

$$\frac{\Delta\varphi_c}{\varphi_c} = \frac{(\varphi_c)_i - (\varphi_c)_0}{(\varphi_c)_0} \,, \tag{6}$$

where $(\varphi_c)_i$ is the coating loss angle as measured after annealing step i and $(\varphi_c)_0$ is the coating loss angle value as measured after the first annealing at 500 °C, taken as reference. Figures 4(b) and (c) show the relative coating loss angle variation as a function of the coating crystalline fraction, for the so-called *butterfly* and *mixed* vibrational modes of different shapes [27]. Indeed, as shown by figure 4(a), in all our $(\varphi_c)_i$ data series we observe a branching of butterfly and mixed modes, likely due to a systematic effect of the raw, coated edge of the sample [15, 27, 28]. However, as figures 4(b) and (c) show, such branching does not affect the observed general trend of the coating loss angle against annealing, which is the same for all modes, and can then be neglected. Thus, the coating loss angle of all modes decreases with the increase of the coating crystalline fraction with an optimum point at annealing step 3, that is, at around 12 h of treatment at 630 °C and with a crystalline fraction of about 5%. At this point the coating loss angle is 10%–20% lower with respect to the standard annealing procedure at 500 °C. A further increase of the crystalline fraction results in a steep increase of the coating loss angle.

3.5. Scattering losses

The presence of a crystalline fraction may increase optical scattering losses in the treated coatings. To quantify this aspect we measured the Total Integrated Scattering (TIS) of the series of K samples with an Internal Diffuse Reflectance Accessory (IDRA-2500) mounted on a Cary

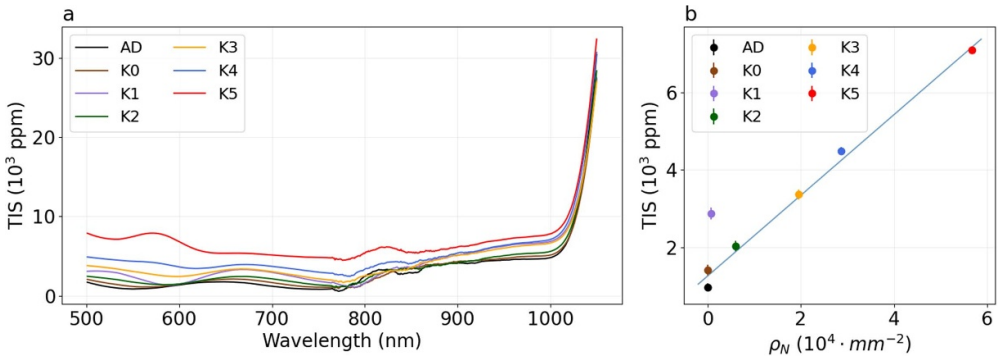

Figure 5. (a) TIS spectrum of as-deposited (AD) coating on silicon and K samples. (b) TIS at 532 nm vs. areal grain density ρ_N of K samples.

5000 UV–Vis–NIR Spectrophotometer. Measurements were carried out in a reflection geometry with an incident angle of 8° in order to direct the specular reflection towards a dumper and measure only the diffusely scattered light. We calculated the TIS as the ratio of the integrated diffuse reflected intensity P_D to the total incident power P_0:

$$\mathrm{TIS} = \frac{P_D}{P_0}\,. \tag{7}$$

Results obtained for the wavelength range 500–1100 nm are shown in figure 5(a): the crystallized grains produce an increase of the TIS over all the measured spectral range. We are especially interested at the wavelength at which GW interferometers work, i.e. 1064 nm. However, since the Si substrate of the K samples is transparent in the infrared range, measurements at 1064 nm may be affected by a contribution from the back surface of the substrate, as can be seen from the steep increase of the TIS between 1000 and 1100 nm in figure 5(a). For this reason, in order to quantify the amount of scattering caused by the crystalline grains in the coating, we instead performed a quantitative TIS analysis at the half-wavelength 532 nm. We assigned to these values the standard deviation of the TIS values measured between 515 and 545 nm as measurement error. Experimental TIS values are between ∼1000 ppm, for samples with no crystallization, and ∼7000 ppm, for the most crystallized sample K5.

The TIS is found to correlate well with the areal grain density ρ_N, as shown in figure 5(b). This behaviour is likely to be attributed to the fact that the crystalline grains are platelet-like-shaped with a typical size equal to or greater than the wavelength, so that TIS is essentially proportional to the surface area of the coating consisting of crystal grains. By fitting the data of figure 5(b) to a linear dependency we obtain:

$$\mathrm{TIS[ppm]} = \alpha + \beta \cdot \rho_N\,, \tag{8}$$

with $\alpha = (1260 \pm 140)$ and $\beta = (1040 \pm 40) \times 10^{-4}\,\mathrm{mm}^2$. In particular, the TIS at 532 nm for the sample K3 with the lowest mechanical losses is 3360 ppm. At 1064 nm the wavelength is comparable to the average grain size found in our samples so that Mie scattering should hold. In this case, the TIS is weakly dependent on the wavelength (as confirmed by figure 5(a)), so

we can conclude that this is also the TIS level due to the crystalline fraction that should be be expected from the sample K3 at 1064 nm.

4. Discussion

As observed in previous works and throughout the present study, thermal treatments carried out at sufficiently high temperatures and/or for a sufficiently long duration induce crystallization in amorphous Ta_2O_5-coatings. In our study we confirmed the crystallization process that occurs through the nucleation and growth of large grains extending throughout the entire thickness of the coatings (for the 500 nm thick samples considered here). These grains are single-crystalline, randomly oriented, with an areal density and an average size that depend on the duration of the thermal treatment. Contrary to conventional wisdom, our results show that a small crystallized volume can be beneficial in terms of mechanical losses. In our study, an optimal crystalline volume fraction of about 5% (corresponding to a 12 h treatment at 630 °C) caused a 10%–20% reduction in coating loss angle across all measured resonance modes with respect to their initial value $\sim 4.5 \times 10^{-4}$ rad or more for the frequency range explored in figure 4, which is typical for Ta_2O_5 coatings annealed according to standard recipes (see [8] for a review).

It is known that as-deposited amorphous coatings are in a non-relaxed state. The objective of standard annealing treatments is simply to allow the amorphous structure to reach a more relaxed state characterized by lower mechanical losses. It is important to emphasize that in previous studies, samples similar to those examined here were annealed at 600 °C for 10 h or at 500 °C for 50 h without showing any signs of crystallization or reducing mechanical loss of the coating [17]. In other words, as long as the samples remain completely amorphous, the coating loss angle after a sufficiently long annealing reaches a stable minimum value which does not decrease even after prolonged thermal treatment. Instead, in our case, starting from *an already relaxed* amorphous sample we show that the mechanical losses can be lowered beyond this limit due to the presence of a small crystallized fraction. This suggests that the reduction in mechanical losses of coatings observed in this work should be ascribed to an additional stabilization due to the formation of a crystalline volume inside our coating samples, and not by a mere relaxation of their amorphous structure alone.

Our results are also in line with recent findings in other materials such TiO_2:Ta_2O_5 [29], GeO_2:TiO_2 [30] and SiO_2:TiO_2 [31] for which low values of the mechanical losses and/or coating thermal noise were observed after a prolonged annealing and in presence of crystallization. The systematic study hereby reported suggests that the stabilization mechanism due to the crystalline fraction may be responsible for the low mechanical losses also in those cases.

On the other hand, at higher values of the crystalline fraction, the coating mechanical losses increase significantly. This indicates that two mechanisms are likely at play: one is dominant at low grain densities and stabilizes the coating structure, while a second one introduces additional losses at high grain concentrations. The optimal grain distribution corresponds to minimal coating mechanical losses. However, the origin of these two contributions remains to be understood. Furthermore, the crystalline fraction is also responsible for increased scattering losses (a typical value of several thousands of ppm in this work), which linearly depend on the areal grain concentration.

Finally, from the point of view of possible applications, it should be mentioned that the average grain size and areal density depend in a different way on the annealing temperature

and duration [32]. We therefore suggest that by extensively exploring the coating grain nucleation process and growth kinetics it could be possible to design some engineered annealing procedures in order to provide samples with a tailored grain size distribution and density. This would open up the possibility to realize coatings with improved mechanical properties, while minimizing the effect of the scattering at the same time. This will be the object of a forthcoming research work.

5. Conclusions

In this work we studied the effect of partial crystallization on the mechanical and optical properties of amorphous Ta_2O_5 thin films produced by using IBS technique, with a perspective application to GW interferometers' mirror coatings. Using optical microscopy, GIXRD and micro-Raman spectroscopy to analyze the crystallized volume of coatings at different thermal treatment durations, we showed that a small amount of crystalline fraction, on the order of a few percent in volume, leads to a decrease in mechanical losses of the coating. However, higher crystalline fractions lead to increased mechanical losses, so that an optimal annealing protocol exists for minimizing the coating loss angle. These findings suggest that, at least from the point of view of the mechanical performances, there is room to perfect the current standard annealing procedures for Ta_2O_5-based thin films of GW interferometers' mirror coatings. On the other hand, the crystalline grains are responsible for a large increase of optical scattering, which needs to be kept under control.

Both the mechanical and optical phenomena hereby reported are strongly dependent on the microscopic structure of the crystalline suspension, so we believe that there is room for improvement: on one hand, by investigating how different micro-structures impact on the optical and mechanical losses; on the other hand, by studying how the microstructure can be controlled by engineering the annealing process. We suggest that such a *high-precision annealing* protocol could pave the way to coatings with improved properties, with the potential of a considerable added value for GW interferometers to an already available coating technology.

Data availability statement

All data that support the findings of this study are included within the article (and any supplementary files).

Acknowledgments

The authors gratefully acknowledge the support of the Agence Nationale de la Recherche (ANR) through Grant No. ANR-18-CE08-0023 (Project ViSIONs). V M and N B gratefully acknowledge the support of the Italian MUR through the national project PNRR—ETIC. N B gratefully acknowledges also the support of the Italian MUR Departments of Excellence Grant 2023-2027 'Quantum Frontiers'.

ORCID iDs

Valeria Milotti https://orcid.org/0000-0003-4732-1226
Marco Bazzan https://orcid.org/0000-0002-1451-1368
Massimo Granata https://orcid.org/0000-0003-3275-1186
Francesco Piergiovanni https://orcid.org/0000-0001-8063-828X

References

[1] The LIGO Scientific Collaboration *et al* 2015 Advanced LIGO *Class. Quantum Grav.* **32** 074001
[2] al Acernese F *et al* 2014 Advanced Virgo: a second-generation interferometric gravitational wave detector *Class. Quantum Grav.* **32** 024001
[3] Akutsu T *et al* 2019 Kagra: 2.5 generation interferometric gravitational wave detector *Nat. Astron.* **3** 35–40
[4] Punturo M *et al* 2010 The Einstein telescope: a third-generation gravitational wave observatory *Class. Quantum Grav.* **27** 194002
[5] Reitze D *et al* 2019 Cosmic explorer: the US contribution to gravitational-wave astronomy beyond LIGO (arXiv:1907.04833)
[6] Reid S and Martin I W 2016 Development of mirror coatings for gravitational wave detectors *Coatings* **6** 61
[7] Craig K *et al* 2019 Mirror coating solution for the cryogenic Einstein telescope *Phys. Rev. Lett.* **122** 231102
[8] Granata M *et al* 2020 Amorphous optical coatings of present gravitational-wave interferometers *Class. Quantum Grav.* **37** 095004
[9] Saulson P R 1990 Thermal noise in mechanical experiments *Phys. Rev.* D **42** 2437–45
[10] Levin Y 1998 Internal thermal noise in the LIGO test masses: a direct approach *Phys. Rev.* D **57** 659–63
[11] Callen H B and Greene R F 1952 On a theorem of irreversible thermodynamics *Phys. Rev.* **86** 702–10
[12] Granata M *et al* 2020 Progress in the measurement and reduction of thermal noise in optical coatings for gravitational-wave detectors *Appl. Opt.* **59** A229
[13] Cole G D *et al* 2023 Substrate-transferred GaAs/AlGaAs crystalline coatings for gravitational-wave detectors *Appl. Phys. Lett.* **122** 110502
[14] Travasso F, Amico P, Bosi L, Cottone F, Dari A, Gammaitoni L, Vocca H and Marchesoni F 2007 Low-frequency internal friction in silica glass *Europhys. Lett.* **80** 50008
[15] Lumaca D *et al* 2023 Stability of samples in coating research: from edge effect to ageing *J. Alloys Compd.* **930** 167320
[16] Teran A V, Bill A and Bergmann R B 2010 Time-evolution of grain size distributions in random nucleation and growth crystallization processes *Phys. Rev.* B **81** 075319
[17] Amato A *et al* 2018 High-reflection coatings for gravitational-wave detectors: state of the art and future developments *J. Phys.: Conf. Ser.* **957** 012006
[18] Joseph C, Bourson P and Fontana M D 2012 Amorphous to crystalline transformation in Ta_2O_5 studied by Raman spectroscopy *J. Raman Spectrosc.* **43** 1146–50
[19] Umari P and Pasquarello A 2003 First-principles analysis of the Raman spectrum of vitreous silica: comparison with the vibrational density of states *J. Phys.: Condens. Matter* **15** S1547–52
[20] Letizia Terranova M L, Guglielmotti V, Orlanducci S, Sessa V, Tamburri E and Rossi M 2009 Preparation and functional characterizations of Ta_2O_5 deposits organized at the micro-and nano-scale *ECS Trans.* **25** 1153
[21] Kim N and Stebbins J F 2011 Structure of amorphous tantalum oxide and titania-doped tantala: ^{17}O NMR results for sol–gel and ion-beam-sputtered materials *Chem. Mater.* **23** 3460–5
[22] Xu M, Chen J, Wen Y, Du J-H, Lin Z and Peng L 2020 ^{17}O solid-state NMR Studies of Ta_2O_5 nanorods *ACS Omega* **5** 8355–61
[23] Nowick A and Berry B 1972 *Anelastic Relaxation in Crystalline Solids* (Elsevier) pp 582–602
[24] Li T *et al* 2014 Measurements of mechanical thermal noise and energy dissipation in optical dielectric coatings *Phys. Rev.* D **89** 092004
[25] Cesarini E, Lorenzini M, Campagna E, Martelli F, Piergiovanni F, Vetrano F, Losurdo G and Cagnoli G 2009 A "gentle" nodal suspension for measurements of the acoustic attenuation in materials *Rev. Sci. Instrum.* **80** 053904
[26] Granata M *et al* 2022 Optical and mechanical properties of ion-beam-sputtered MgF_2 thin films for gravitational-wave interferometers *Phys. Rev. Appl.* **17** 034058
[27] Cagnoli G *et al* 2018 Mode-dependent mechanical losses in disc resonators *Phys. Lett.* A **382** 2165
[28] Amato A *et al* 2022 Systematic error in the internal friction measurement of coatings for gravitational wave detectors *Phys. Rev.* D **106** 082007
[29] Murray P, Bassiri R, Bell A, Martin I, Reid S, Robie R, Rowan S, Steinlechner J and Vine D 2017 *Glasgow update II: cryogenic coatings* G1700874-v1 LIGO Technical Note

[30] Vajente G *et al* 2021 Low mechanical loss TiO_2:GeO_2 coatings for reduced thermal noise in gravitational wave interferometers *Phys. Rev. Lett.* **127** 071101
[31] McGhee G I *et al* 2023 Titania mixed with silica: a low thermal-noise coating material for gravitational-wave detectors *Phys. Rev. Lett.* **131** 171401
[32] Spinella C, Lombardo S and Priolo F 1998 Crystal grain nucleation in amorphous silicon *J. Appl. Phys.* **84** 5383–414